ACS NANO

www.acsnano.org

Article

All-Printed MXene-Based Springs for Concurrent Bidirectional Hand Motion Capture

Chendong Zhao, Jimei Liu, Bingxue Zhang, Xinyu Liu, Yuanjie Jiang, Qinglong He, Mengzhou Liao, Yan Zhao, Caofeng Pan, Valeria Nicolosi, and Chuanfang Zhang*

Cite This: *ACS Nano* 2026, 20, 14479−14487

Read Online

ACCESS | Metrics & More | Article Recommendations | Supporting Information

ABSTRACT: Accurately capturing hand movements remains a challenge because the skin undergoes stretching, compression and bending at the same time, yet most flexible sensors respond only to tension. Achieving high sensitivity and a wide range often means making the sensor thick, which causes the sensing layer to shift under complex deformations and distorts the signal. Here, we address this by placing the strain-accommodating space within a plane parallel to the strain direction. Using a MXene/polyurethane ink with glycerol as a molecular bridge, we create a dense hydrogen-bonding network that enables high-resolution printing of a planar spring architecture. The resulting all-printed sensor achieves a gauge factor of 83.7 across a linear bidirectional range of ±60% strain. With just two sensors, we track and decode complex wrist motions with ±10° accuracy. When attached to finger joints, they enable real-time, dexterous control of a virtual hand. This work provides an alternative approach for skin strain capture through synergistic innovation in materials and architecture.

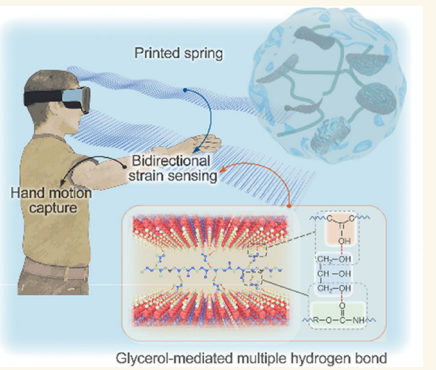

KEYWORDS: *MXene ink, 3D printing, wearable sensors, hand motion tracking, bidirectional strain sensing*

1. INTRODUCTION

Precise sensing of human hand movements is critical in fields such as medical rehabilitation, human−computer interaction, and sports science.[1,2] Current methods like optical motion capture,[3] IMUs,[4] and EMG[5,6] can recognize hand motions but are limited by bulkiness, cost, resolution, and environmental interference.[7,8] Flexible, skin-conformable strain sensors offer a promising alternative.[9,10] However, hand motion involves complex skin deformation patterns where tensile, compressive, and bending strains coexist.[11,12] This demands sensors capable of faithfully capturing both tension and compression simultaneously—a key step toward next-generation wearable motion interfaces.

Recent efforts have focused on structural design to address this, creating micro/nanoarchitectures that accommodate both deformation modes.[13−15] Porous or foam structures enable pore closure under compression and opening under tension, producing opposite resistance changes.[16] Bioinspired gradient structures use modulus-graded layers to generate differential strain distributions during bending, enabling directional response.[17] Other strategies employ predefined spring or microarch geometries to distinguish between tensile and compressive loads.[18] While these approaches can generate bidirectional signals, they typically place the strain-accommodating space perpendicular to the strain direction. Achieving higher sensitivity and wider range often requires increased device thickness, causing the sensing layer to shift during bending and leading to signal distortion under complex deformations.[19]

An ideal solution would place the strain-accommodating space within a plane parallel to the strain direction, enabling an ultrathin sensor that conforms to skin wrinkles and faithfully captures surface strain.[20−22] This requires the sensor to form dense electrical pathways that open and close within a limited planar area under strain, which in turn demands molecular-level bond design for efficient strain transfer to conductive nanounits. MXene, with its abundant tunable surface groups and high conductivity, can form rich interactions with elastic polymers and other conductive nanomaterials, enabling effective stress transfer.[23−25] For instance, dynamic Ag−S coordination bonds between silver nanowires and MXene can modulate crack generation and closure, allowing distinct resistance trends under tension.[26] However, such material strategies often involve complex fabrication and remain limited in their ability to detect both tensile and compressive strains simultaneously. Thus, a major challenge lies in integrating material and structural innovations to reconcile the conflicting

Received: November 26, 2025
Revised: April 30, 2026
Accepted: May 1, 2026
Published: May 8, 2026

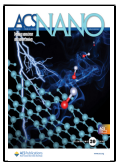

demands of high sensitivity, precision, and range for both tension and compression.

Here, we address this challenge through a combined strategy of structural design and material optimization, achieving high-precision sensing of both tensile and compressive strains within a planar architecture. We first develop a novel MXene/polyurethane (PU) composite ink via hydroxyl-mediated interfacial engineering, introducing glycerol as a bridging agent to strengthen the MXene−PU interface through hydrogen bonding. This not only enhances the mechanical robustness of the composite but also ensures uniform MXene dispersion and creates abundant interfaces capable of withstanding strain. The resulting homogeneous ink enables the faithful fabrication of a designed planar spring structure via high-resolution 3D printing. This architecture places the strain-accommodating space for both tension and compression within the same plane parallel to the strain direction, effectively decoupling sensitivity and sensing range from device thickness, thereby enabling an ultrathin sensor with excellent bidirectional sensing performance. When integrated into a wireless system, these sensors enable the quantitative tracking of multiple hand joints and decoding of complex multi-degree-of-freedom wrist motions using a minimalist sensor configuration, ultimately facilitating real-time control of a virtual hand avatar. This work offers a new perspective on skin strain sensing for human motion and provides a promising solution for applications in teleoperation, rehabilitation diagnostics, and immersive virtual reality.

2. RESULTS AND DISCUSSION

2.1. Material Design Strategy for Synergistic Properties

Achieving high-resolution printing of functional spring structures necessitates an ink that simultaneously possesses excellent conductivity, mechanical elasticity, and dispersion stability. To this end, we utilize the excellent electrical conductivity and unique surface chemistry on MXene to composite with elastic PU to resolve the inherent conflict between conductivity and elasticity at low filler loading. Moreover, the MXene's unique functionalities facilitate the interfacial engineering, allowing the formation of a homogeneous composite ink for subsequent 3D printing, as schematically illustrated in Figure 1a.

We start by describing the synthesis of high-quality MXene flakes. The high-quality Ti_3AlC_2 MAX phase was synthesized with size of around 30 μm (Figure S1). Following the wet etching, the ternary MAX turns to accordion-like multilayered MXene with a high quality, best evidenced by the prominent (00*l*) peaks (Figure S2). Upon LiCl intercalation and mild shaking, the multilayered MXene delaminates into mono- and bilayer MXene flakes, as shown in the transmission electron microscopy (TEM, Figure S3) as well as atomic force microscopy (AFM, Figure S4). The hexagonal, clean flakes with lateral size ~10 μm indicate the high-quality nature of the as-synthesized MXene (inset in Figure S3).

While the hydroxyl groups on MXene surfaces facilitate hydrogen bonding with PU, the resulting bond density and strength are often limited by steric hindrance, leading to compromised mechanical and electrical properties of the composites. To this end, we introduce a strategic material modulation via glycerol-mediated hydrogen bonding to enhance the dispersibility of MXene in the PU matrix. As a small molecule with multiple hydroxyl groups, glycerol serves as a versatile molecular bridge that concurrently forms dense, multisite hydrogen bonds with both MXene and PU chains (Figure 1b). This significantly enhances the interfacial connectivity, leading to improved MXene dispersion uniformity within the polymer matrix (Figure S5), which is crucial for formulating a homogeneous ink that is essential for high printing precision. The superior dispersion mitigates nanofiller agglomeration, thereby facilitating the formation of robust and continuous conductive pathways, which bolsters the overall electrical conductivity of the elastomer.

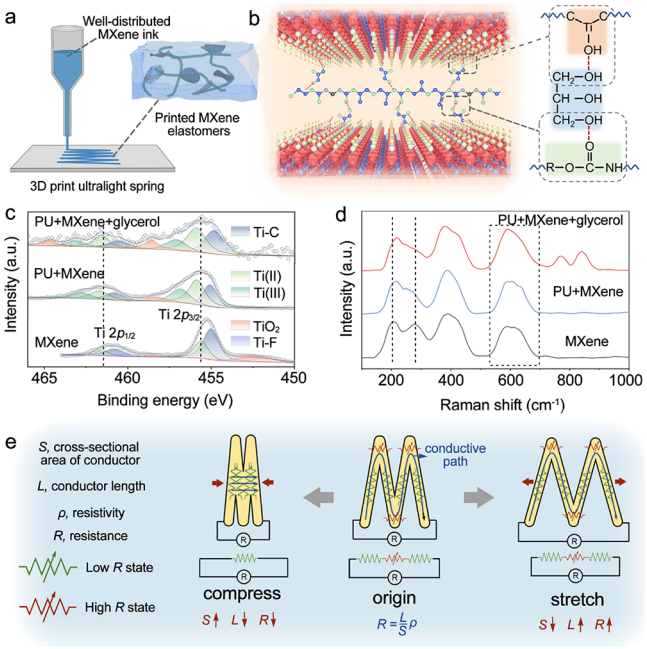

Figure 1. Schematics of (a) the 3D printing process and (b) the interfacial engineering, forming a strong hydrogen bond network in the resultant MXene/PU/glycerol elastomer. (c) Ti 2*p* XPS spectra and (d) Raman spectra of pristine MXene, MXene with PU, and MXene with PU/glycerol. (e) Sensing mechanism and equivalent circuit diagram of the bidirectional strain sensor.

The enhanced interfacial interaction is conclusively evidenced by X-ray photoelectron spectroscopy (XPS). The MXene−PU composite shows a slight shift of the Ti valence state toward higher binding energy against that of MXene alone, indicating weaker interfacial interactions (Figure 1c).[27] However, upon incorporation of a small amount of glycerol, the Ti spectrum undergoes a pronounced shift, suggesting that the chemical environment around Ti atoms changes significantly. This change arises from glycerol-mediated multiple hydrogen bonds at the MXene−PU interface, which modifies the electron cloud density of MXene. This is further validated by Raman spectroscopy (Figure 1d). The spectrum of the MXene/glycerol/PU blend shows a decreased intensity of the peak near 280 cm^{-1} compared with that of pristine MXene, indicative of limited hydrogen bonding. In contrast, after functionalization with glycerol, the sample exhibits a notable change in the relative intensity of the peaks around 600 and 280 cm^{-1}, respectively. This spectral evolution strongly supports the role of glycerol in promoting extensive, multifaceted hydrogen bonding between MXene and PU.[28] Such enhanced interfacial interactions are key to achieving uniform MXene dispersion within the PU matrix (Figures S6 and S7). We note that larger MXene flakes minimize interflake

https://doi.org/10.1021/acsnano.5c20704
ACS Nano 2026, 20, 14479−14487

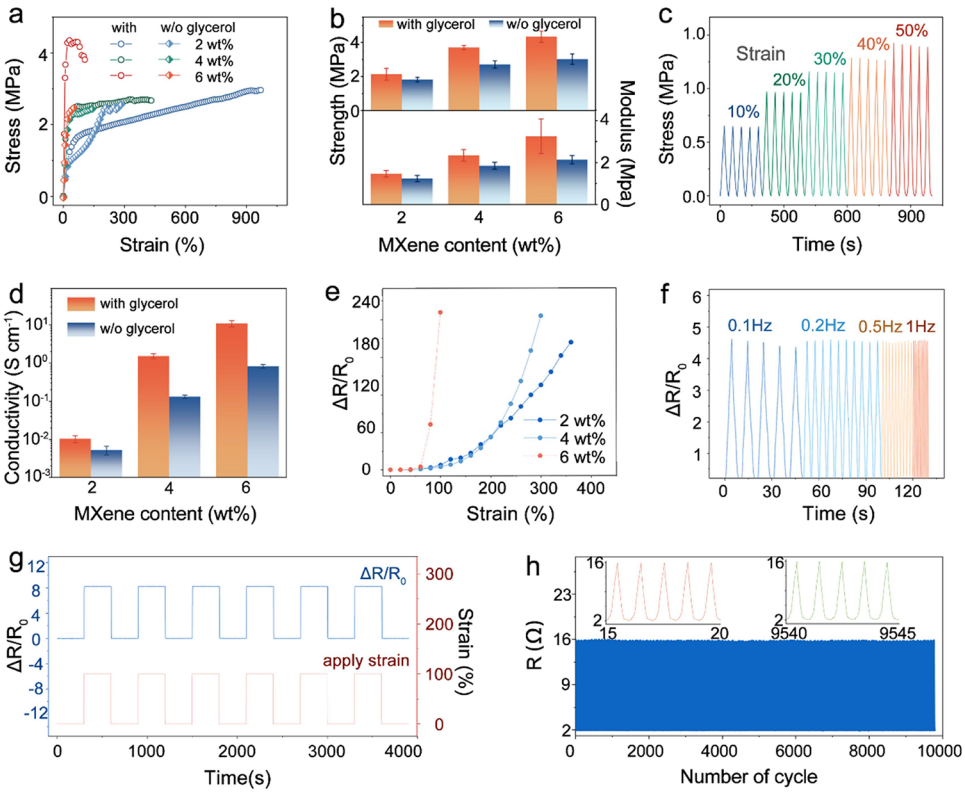

Figure 2. Investigation of the strain-dependent electromechanical properties of MXene/glycerol/PU elastomers. (a) Tensile stress−strain curves of the composite elastomers with different MXene contents and (b) the corresponding statistical modulus and strength. (c) Gradient stability testing of the elastomer with 4 wt % MXene content under various strains. Electromechanical characteristics of elastomers with different MXene contents: (d) resistance change under tensile strain, (e) statistical conductivity, and (f) resistance change response at different strain frequencies. (g) The MXene/glycerol/PU elastomer exhibits excellent response speed and anticreep properties under pulsed strain, attributed to the benzene rings and partial crystallinity in the PU molecular chains. This also endows the elastomer with good cyclic stability (h).

electron hopping resistance, enhancing electrical conductivity at lower MXene loadings, while the strong H-bonding reduces the typical filler-induced degradation of polymer elasticity. As such, the contradiction between conductivity and elasticity at low filler loading is mitigated, allowing the printing of lightweight springs for sensitive strain sensors, as discussed below.

On top of the material design described above, the structural layout also plays an important role in boosting the sensing performance. To this end, we innovate the sensor pattern capable of detecting both positive (tensile) and negative (compressive) strains. This is realized by printing spring-like structures whose electrical response follows the fundamental resistance relation $R = (\rho L)/S$ (where ρ is the resistivity, L is the conductive path length, and S is the cross-sectional area), as illustrated in Figure 1e. Under tensile strain, the spring structure elongates, increasing the conductive path length L while reducing the cross-sectional area S due to Poisson's effect. Both factors contribute to a significant increase in R, enabling reliable detection of positive strain. Conversely, under compressive strain, the predesigned gaps between spring lines progressively close. This shortens the effective conductive path L and increases the contact cross-section S, leading to a clear decrease in R. This bidirectional resistance variation—rising under tension and falling under compression—allows the sensor to distinguish between tensile and compressive deformations accurately and quantitatively within a single, minimalist architecture.

In the stress−strain curves of the MXene/glycerol/PU composites, more MXene corresponds to increased modulus and yield strength at the cost of elongation at break (Figure 2a,b), which can be attributed to the disruption of PU chain entanglement and crystallinity. Achieving an optimal balance between elasticity (for large strain accommodation) and fracture resistance (for structural integrity) is paramount for the targeted bidirectional sensing application. Based on this analysis, the 4 wt % MXene composition is identified as the optimal compromise and selected for further characterization. This composite demonstrates excellent cyclic tensile stability across various applied strains (Figure 2c), confirming its mechanical robustness. The electrical conductivity measurements further validate that 4 wt % MXene is sufficient to induce electromechanical response ($\Delta R/R_0$) in a wide strain sensing range (Figure 2d,e), in sharp contrast to an abrupt resistance surge upon stretching the 6 wt % MXene-based composite, indicative of the brittle fracture behavior in the latter. Even under dynamic straining at various frequencies, the 4 wt % composite maintains undistorted waveforms and consistent signal intensity (Figure 2f), and the rapid response time ensures high-frequency motion capture in the 3D-printed strain sensors.[29−31]

The pulsed strain testing (Figure 2g) confirms this rapid, square-wave-like resistance response with negligible signal creep under constant strain. This exceptional stability arises from the restricted chain mobility imposed by the benzene rings and the partially crystalline domains within the PU backbone. The suitability of the 4 wt % MXene/glycerol/PU

https://doi.org/10.1021/acsnano.5c20704
ACS Nano 2026, 20, 14479−14487

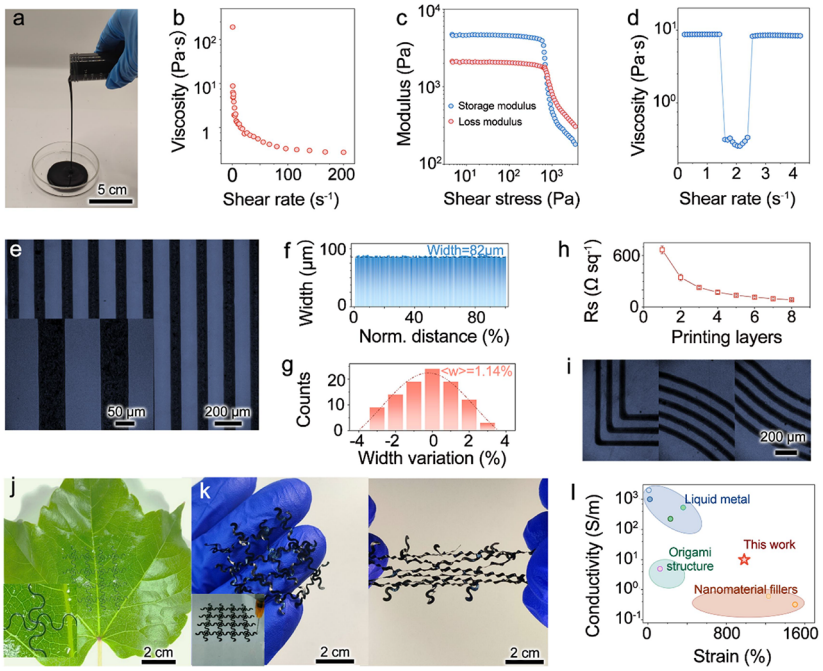

Figure 3. Characterization of the printing characteristics of MXene conductive ink. (a) Optical photograph of the ink demonstrating its homogeneous fluid nature. Rheological measurements of the MXene conductive ink: (b) viscosity as a function of shear rate, (c) storage modulus (G') and loss modulus (G'') as a function of shear stress, and (d) thixotropic behavior. (e) Optical micrograph of printed straight-line arrays, with the inset showing a magnified view. (f) Statistical distribution of printed line widths and (g) standard deviation of the line width distribution. (h) Sheet resistance of printed lines as a function of the number of printed layers. (i) Printed right-angle and curved lines illustrating the uniformity of the ink at corners and bends. (j) Printed lines conforming seamlessly to leaf veins, with the inset showing a magnified view. (k) Printed strain sensor array and its excellent tensile properties. (l) Comparison of the line width and printing precision achieved with the present MXene conductive ink vs results reported in the literature.

composite for practical sensing applications is validated through rigorous long-term cyclic testing (Figure 2h). After 10,000 continuous strain cycles, the composite exhibits exceptional stability, with negligible decay in the resistance response amplitude and no observable waveform distortion. This outstanding durability confirms the formation of stable and elastic conductive pathways within the composite microstructure capable of withstanding repeated mechanical deformation.

2.2. Engineered Rheology for High-Resolution Printing

Having established the MXene/glycerol/PU composite ink with optimal electrical and mechanical properties, we next investigate its rheological behavior to enable high-resolution direct printing of intricate lightweighted springs. The ink exhibits a pronounced non-Newtonian, shear-thinning behavior (Figure 3a), characterized by a sharp viscosity decrease under high shear rates (Figure 3b), a prerequisite for smooth extrusion through fine nozzles. Dynamic oscillatory rheometry further reveals a solid-like gel state at rest (storage modulus G' > loss modulus G'') under low shear stresses. When exceeding a critical yield stress (~400 Pa), G' and G'' decrease sharply, transitioning to a dominant fluid-like state (G'' > G') suitable for extrusion (Figure 3c). The as-formulated ink also demonstrates rapid viscosity recovery upon the removal of the shear force (Figure 3d), suggesting excellent thixotropy that is essential for retaining the extruded filament shape and preventing postdeposition flow.[23,32]

As such, direct extruding of the formulated MXene−PU ink produces uniform lines with an average width of 82 μm (Figure 3e). Statistical analysis confirms exceptional printing resolution and uniformity, yielding a minimal line width variation of only 1.14% (Figure 3f,g). We note that the printing of such fine filaments with remarkable consistency surpasses those of typical 3D printed lines and can be fairly attributed to the (1) controlled ink−substrate interactions and high G' with minimal ink spreading (Figure S8) and (2) robust cohesion within the ink filament, effectively eliminating common defects like line breakage, corner accumulation, or pooling (Figure 3i). We attribute this defect mitigation to strong hydrogen bonding, both within the MXene/glycerol/PU composite (enhancing cohesion) and ink/substrate (promoting adhesion and wetting control) (Figure S9). The height measurement further confirms the precise vertical stacking of MXene/glycerol/PU filaments without significant lateral spreading, as the thickness increases linearly with the number of printed layers in the absence of any plateaus (Figure S10).

The precise 3D printing of MXene−PU ink serves as an efficient building block for the scalable production of ultrafine conductive lines with tailored sheet resistance at ease (Figure 3h). For instance, lightweighted patterns seamlessly adhering to complex microtextured surfaces like leaf veins (Figure 3j), as well as freestanding stretchable arrays (Figure 3k), are printed with excellent conformability. It is worth mentioning that our MXene/glycerol/PU ink simultaneously achieves high printability (evidenced by fine lines with high uniformity), outstanding conductivity, and remarkable stretchability. As quantitatively benchmarked in Figure 3l, this combination of properties surpasses many reported counterparts, such as liquid-metal-based inks and patterns employing origami or nanomaterial fillers, thereby allowing the efficient fabrication of functional microarchitectures like strain-sensing springs.

https://doi.org/10.1021/acsnano.5c20704
ACS Nano 2026, 20, 14479−14487

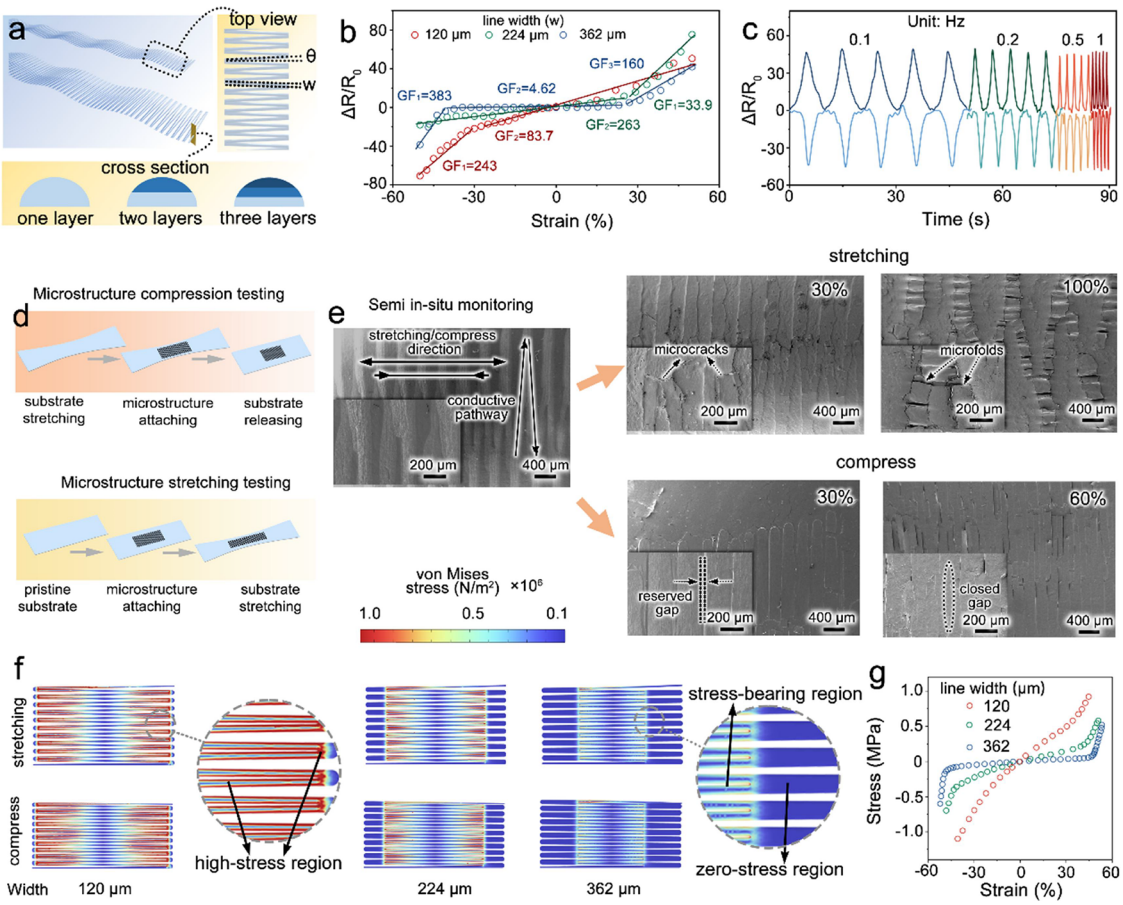

Figure 4. Printed sensors for tensile and compressive strain and their working principles. (a) Schematic illustration of the printed 2D spring structure. Key parameters directly influencing sensing performance include the line angle (θ) and line width (w). To enhance the gauge factor (GF) for compressive strain, a multilayer printing strategy with gradually decreasing ink conductivity from top to bottom layers was employed. (b) Resistance−change curves of sensors with different line widths under tensile and compressive strain. (c) Performance testing under tensile and compressive strain at various frequencies. (d) Schematic of the semi in situ tensile/compressive microstructure observation. (e) SEM images illustrating microstructural changes under tensile and compressive strain. (f) Finite element simulation (e.g., COMSOL) of stress distribution in devices with different line widths under tensile and compressive strain and (g) the corresponding simulated stress−strain curves of the spring structure with different line width.

2.3. Structural Optimization of the Spring Sensor

Sensing negative strain requires incorporated strain accommodable space in the design; achieving high sensitivity relies on sufficiently long conductive paths for sensing. As such, we fabricate lightweighted springs as the core bidirectional strain sensing element through 3D extrusion printing of MXene/PU/glycerol ink. The as-printed spring can be supported on a single hair (Figure S11). For the printed springs, the wire angle (θ) and line width (w) are the primary factors determining the sensor's response (Figure 4a).

Reducing θ from 3° to 1° significantly increases the initial gauge factor (GF) for both tensile and compressive strains (Figure S12). However, at θ = 1°, excessive line proximity induces mechanical instability (e.g., line adhesion or buckling under compression), leading to unreliable sensing performance. Instead, the spring sensitivity and structural integrity are well optimized when θ = 2°. On the other hand, decreasing the printed line width from 362 to 120 μm dramatically enhances the initial GF (from ∼3 to ∼83.7) as well as the linearity (R^2 from 0.74 to 0.95, Figure 4b and Figure S13) for both tensile and compressive strains. This confirms that finer conductive traces enable superior sensitivity and linearity in bidirectional sensing.

We further implement a conductivity-graded multilayer printing strategy to further amplify the compressive strain response. Such a design features a higher MXene concentration in upper layers and lower MXene in the bottom layer (Figure 4a). When the spring is subjected to tension, cracks initiate preferentially in the more brittle, higher-MXene-content top layer, amplifying resistance increase (higher tensile GF). Upon compression, the sequential contact of the highly conductive upper layers efficiently establishes increasing number of low-resistance percolation pathways, enhancing resistance and leading to much higher compressive GF than that of conventional architectures (Figure S12). The optimized spring sensor (θ = 2°, W = 120 μm, gradient structure) demonstrates robust and reliable operation across diverse dynamic conditions. For example, the 3D-printed spring exhibits well-defined, reproducible resistance signals that accurately track applied tensile/compressive strain profiles over various amplitudes and frequencies (Figure 4c and Figure S14), confirming its suitability for capturing complex, time-varying deformations.

The microscopic analysis provides critical insights into the sensing mechanism of the printed spring sensor. As illustrated in Figure 4d, the strain constructs were mounted on a

https://doi.org/10.1021/acsnano.5c20704
ACS Nano 2026, 20, 14479−14487

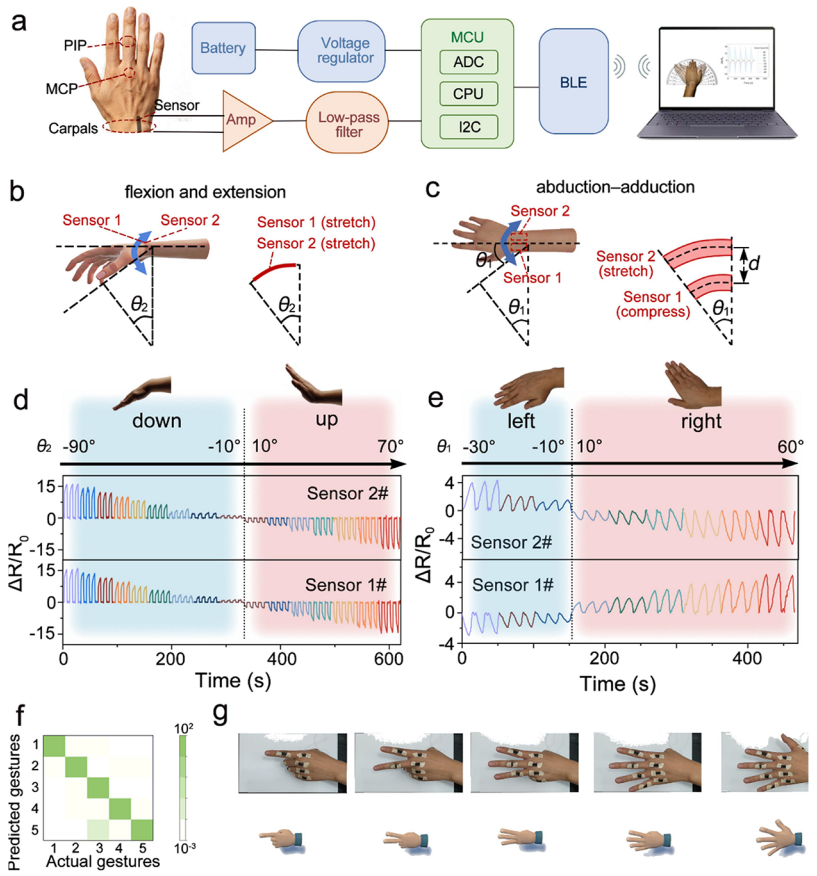

Figure 5. Validation of the hand motion sensing system. (a) Schematic illustration of the DoF in human hand joints and the working principle of the wireless signal transmission system. Schematic and working principle for distinguishing (b) flexion and extension and (c) lateral (left−right) flexion of the wrist joint using two parallel sensors. Actual test data for (d) flexion and extension and (e) lateral (left and right) flexion. Operation demonstration for the VR virtual hand (f) and the corresponding confusion matrix (g).

prestretched VHB substrate using fixed clamps, enabling semi in situ microscopic observation during deformation. Under tensile strain, crack initiation preferentially occurs at the line junctions—sites of inherent stress concentration. Further strain promotes uniform crack propagation along the conductive paths (Figure 4e and Figure S15a). The resulting reduction in the effective conductive cross-section, coupled with an increase in electron tunneling barriers, drives the resistance increase, thereby explaining the observed high sensitivity and linearity. In contrast, under compressive strain, the predesigned gaps between adjacent spring lines progressively decrease (Figure 4e). At approximately 60% compressive strain, these gaps close completely, maximizing the conductive contact area and minimizing resistance. Further compression leads to surface wrinkling and resulting device instability (Figure S15b).

COMSOL simulations corroborate that finer printed lines promote a more uniform distribution of both tensile and compressive stresses, mitigating localized stress concentration (Figure 4f). The insets illustrate that the 120 μm line width enables a more uniform strain distribution across the structure, leading to a superior sensing range, in contrast to the limited and localized strain observed in the 362 μm counterpart. As such, a stable and linear resistance change is achieved, enabling high sensitivity while extending the reliable sensing range in the as-printed spring sensors (Figure 4g). Critically, the distinct yet complementary responses under tension and compression enable robust bidirectional strain sensing within a single, as-printed device—a capability unattainable by conventional unidirectional sensors based on serpentine or straight-line layouts, which typically require spatially distributed sensor arrays to detect multiaxial deformations. By synergizing material and architectural design, our sensor overcomes this fundamental limitation, providing a minimalist yet high-performance solution for accurate motion decoding. This advance not only establishes a new paradigm in wearable sensing design but also paves the way for lightweight, highly integrated systems in real-world applications such as immersive teleoperation and personalized rehabilitation.

2.4. Precision Hand Motion Capture Enabled by Bidirectional Sensing

We further design a strain-sensing array aiming to achieve more accurate perception of bending radii and angles (Figure S16). By analyzing the relative R changes in both the collective response of the array and the individual resistances during bending, the corresponding bending angles and radii can be derived through computational fitting—marking the first successful decoupling of these two parameters (Figure S17). In this configuration, strain sensors are arranged in parallel. During bending, sensors on the outer and inner sides experience different strain levels. When the bending radius is constant and the bending angle increases, the strain ratio between the outer and inner sensors remains consistent, but a greater number of sensors are engaged in the strain field. This relationship is summarized by the formula:

https://doi.org/10.1021/acsnano.5c20704
ACS Nano 2026, 20, 14479−14487

$$\theta \propto \sum_{k=1}^{5} (\Delta R/R_0)_k \quad (1)$$

where θ is the bending angle, k corresponds to the sensor index in Figure S15, and $\Delta R/R_0$ is the relative resistance change of each sensor.

Conversely, when the bending angle is fixed and the bending radius decreases, the number of sensors involved remains unchanged, but the strain ratio between the outer and inner sensors increases. This relationship is summarized by the formula $r \propto [(\Delta R_{top}/R_{0top})/(\Delta R_{bottom}/R_{0bottom})]$, where r is the bending radius. R_{top} and R_{bottom} denote the sensors positioned farther from and closer to the center of curvature, respectively. By performing linear fitting on the scatter plot of ratios from sensors at different positions, the slope of the resulting line directly indicates the bending radius r (Figure S17f).

Accurately capturing of hand motions holds broad applications in fields such as hand rehabilitation therapy, robot manipulation, and virtual reality. However, the hand's multiple DoFs pose a significant challenge for high-fidelity monitoring—particularly in achieving lightweight, noninvasive sensing without interfering with natural movement. As such, we employ the as-printed strain-sensing array to semi-quantitatively detect the flexion−extension and abduction−adduction of the carpal joint. Sensors were also mounted on the proximal interphalangeal (PIP) and metacarpophalangeal (MCP) joints. The acquired signals were conditioned via an operational amplifier circuit, digitized through a microcontroller's analog-to-digital converter (ADC), and wirelessly transmitted to mobile devices (e.g., computers and smartphones) via a Bluetooth module for real-time motion monitoring (Figure 5a, Figures S18−S20, and Video S1).

We indeed achieve semiquantitative monitoring of wrist motion based on the relative strain responses from two parallel sensors mounted at the wrist (Figure S21). During flexion and extension, both sensors exhibit synchronous strain: they encounter positive strain during flexion and negative strain during extension (Figure 5b). The flexion and extension angle (θ_2) can be directly read from the relative resistance change of each sensor. Experimental results confirm this behavior, showing that the sensors distinguish flexion and extension angles with a resolution up to ±10° (Figure 5d). These strain values exhibit a linear relationship with the bending angle (Figure S22a).

In contrast, during left−right lateral bending (abduction−adduction), these two sensors display opposing strain responses. For instance, when the wrist bends to the left, the left sensor undergoes negative strain, while the right one experiences positive strain (Figure 5c). We define ε_1 and ε_2 as the strains on two sensors during lateral flexion. The lateral flexion angle (θ_1) can be thus written as

$$\tan \theta_1 = \frac{\varepsilon_2(\varepsilon_2 - \varepsilon_1)}{\varepsilon_1 d} \quad (2)$$

where d represents the distance between the central axes of the two sensors. The ratio of their strain values correlates linearly with the lateral bending angle (Figure 5e), enabling distinction of lateral movements within ±10° (Figure S22b). These findings demonstrate that two complementary sensors operating in differential modes allow effective semiquantitative assessment of the multi-degree of freedom of wrist motions.

Finally, our minimalist printed sensor solution enables multi-DoF hand motion capture with a reduced number of sensors, offering a viable approach for real-time virtual hand control in immersive VR environments. As illustrated in Figure S23, by attaching two lightweighted, as-printed springs to the MCP and PIP joints, respectively, real-time monitoring of finger flexion is realized. The predicted finger joint angles derived from sensor responses closely match the actual values, with scatter data following a strong linear trend ($R^2 > 0.98$). Over 80% of the predictions fall within a ±5° deviation from the true angles, confirming high measurement accuracy. Further extending our spring sensors to 10 MCP and PIP joints, significantly enhanced and repeatable signal variations are observed during hand opening and closing, enabling comprehensive gesture capture (Figure S24). Building on these results, we deployed the system for VR-based human−machine interaction using a self-developed, portable module for signal acquisition and wireless communication, worn on the forearm to enable real-time capture (Figure 5f,g).

This robust and lightweight sensing system, capable of resolving both finger and wrist motions with high fidelity, provides a practical platform for real-time virtual body gesture capturing in immersive VR environments, opening avenues for applications in rehabilitation, teleoperation, and human−computer interaction, to name just a few.

3. CONCLUSIONS

To summarize, this work overcomes a fundamental limitation in wearable motion capture—the inability of unidirectional strain sensors to resolve multiaxis deformations at single points—by synergizing material innovation with micro-architectural design. We introduce the hydroxyl-mediated interfacial bonding to boost the dispersibility of large-size MXene flakes in the elastic matrix, forming homogeneous conductive inks of MXene/glycerol/PU for subsequent high-resolution printing of elastic conductors. The COMSOL simulations guide the efficient spring architecture design, with predefined strain zones and gradient conductivity achieved simultaneous. Consequently, our all-printed spring sensors allow highly sensitive bidirectional sensing (GF = 83.7, 0−60% strain), outperforming the rest known conventional strain sensor in terms of functionality or sensitivity. We demonstrate the multi-DoF, bidirectional hand motion capture using two sensors, establishing a robust platform for joint-angle quantification (±10° error) and dexterous VR control. This work bridges critical gaps in human−machine interfaces, with immediate applications in rehabilitation diagnostics, VR interaction, and soft robotics. However, further structural design is required to address complex strain fields such as torsion or shear.

4. METHODS

4.1. Materials

Titanium powder (99.5%), aluminum powder (99.5%), graphite (99%), glycerol (AR), hydrochloric acid (37 wt %, AR), lithium fluoride (Alfa, 99.85%), hydrofluoric acid (Alfa, ≥40%), *N*,*N*-dimethylformamide (DMF, 99.9%), and polyurethane (PU, 500 mesh, Guangyuan Plastic Products Co., Ltd., Guangzhou) were used as purchased without further purification.

https://doi.org/10.1021/acsnano.5c20704
ACS Nano 2026, 20, 14479−14487

4.2. Methods

4.2.1. Synthesis of the Ti_3AlC_2 MAX Phase. Graphite powder, titanium powder, and aluminum powder were mixed at a molar ratio of 1.8:3.1:2 and ball-milled for 18 h. The mixed powder was then heated to 1500 °C under an argon atmosphere and held for 3 h. After natural cooling, the resulting bulk material was crushed into particles below 38 μm. The particles were then etched with 9 M hydrochloric acid at 40 °C for 24 h. After the reaction, the product was washed with deionized water until the pH reached neutrality followed by vacuum drying at 80 °C for 6 h to obtain the MAX phase powder.

4.2.2. Wet Etching of the $Ti_3C_2T_x$ MXene. One gram of the synthesized MAX powder was slowly added to 20 mL of an etching solution composed of HF, HCl, and deionized water mixed at a volume ratio of 1:6:3. The reaction was carried out under stirring at 35 °C for 48 h. Upon completion, the product was washed repeatedly with deionized water until the pH reached 6.

4.2.3. Delamination of $Ti_3C_2T_x$ MXene. To delaminate the etched MXene, lithium-ion intercalation was employed. The etched MXene was added to a 20 mg/mL LiCl solution and stirred at 35 °C for 18 h. After the reaction, residual LiCl was removed by repeated centrifugation (3500 rpm) and washing with deionized water. The mixture was then manually shaken for 1 h to obtain a delaminated MXene dispersion. To prepare the delaminated MXene ink, the upper dispersion was first collected by centrifugation at 3500 rpm for 10 min. Subsequently, the lower sediment was harvested by centrifugation at 12,000 rpm for 1 h, yielding the MXene ink. To determine the solid content (C) of the MXene ink, a known mass (M) of the ink was vacuum-dried at 80 °C for 12 h. The weight of the dried ink (m) was measured, and the solid content was calculated using the formula $C = m/M$. To exchange the dispersion solvent of the MXene ink to DMF, a portion of the ink was diluted with a large volume of DMF and manually shaken for 30 min. This was followed by centrifugation at 12,000 rpm for 1 h. The supernatant was discarded, and the process (redispersion in fresh DMF and centrifugation) was repeated three times, resulting in DMF-dispersed MXene ink.

4.2.4. Characterization of MXene. The structure of MXene was confirmed by XRD (Cu Kα radiation, λ = 1.54178 Å, D/max 2550 V, Rigaku) and Raman spectroscopy (Horiba LabRAM HR Evolution), the morphology was studied by SEM (ZEISS Sigma 300) and TEM (Japan-JEOL-JEM 2100Plus), and the elemental composition was characterized by EDS (OXFORD X-act one) and XPS (Thermo Scientific ESCALAB Xi+).

4.3. 3D Printing

4.3.1. Ink Preparation. A 37 wt % polyurethane (PU) solution in water was first mixed with a specific amount (5 wt %) of glycerol. Subsequently, a predetermined amount of the MXene ink was added, and the mixture was homogenized using a mixer for 1 h to obtain the printing ink. The 3D printing process for fabricating high-toughness hydrogel structures was performed using a programmable three-axis pneumatic robotic deposition system (SM500ΩX-3ASS, MUSASHI) controlled by painting software (MuCAD, MUSASHI). Ultrafine printing was achieved using a 34G nozzle under an air pressure of 200−300 kPa. After printing, the structures were vacuum-dried at 50 °C for 24 h to yield the printed sensors.

4.3.2. Gesture Signal Acquisition. A custom measurement system based on an Arduino Uno was developed to simultaneously acquire resistance values from five strain sensors. Each sensor was configured in a voltage divider circuit by connecting it in series with a 100 kΩ precision fixed resistor between a 5 V supply and ground. The analog input pin of the Arduino sampled the voltage at the node between the fixed resistor and the sensor. All five channels were scanned sequentially, with each channel sampled 10 times and averaged to suppress high-frequency noise.

■ ASSOCIATED CONTENT

Data Availability Statement

The data can be acquired upon email contact with the corresponding author.

Supporting Information

The Supporting Information is available free of charge at https://pubs.acs.org/doi/10.1021/acsnano.5c20704.

SEM and XRD results of MAX and MXene; TEM and AFM results of MXene; dynamic light scattering (DLS) results of inks prepared under different conditions; surface energy of the ink and its contact angle with the substrate; statistics of printed line thickness and corresponding optical images; cyclic response, response time, and hysteresis curves of the printed sensor under varying strain levels; arrangement and response signals of the strain sensor array; and statistical data of finger bending angles (PDF)

Video showing real-time hand motion monitoring and human−robot interaction (MP4)

■ AUTHOR INFORMATION

Corresponding Author

Chuanfang Zhang − *College of Materials Science & Engineering, Sichuan University, Chengdu, Sichuan 610065, China*; orcid.org/0000-0001-8663-3674; Email: chuanfang.zhang@scu.edu.cn

Authors

Chendong Zhao − *College of Materials Science & Engineering, Sichuan University, Chengdu, Sichuan 610065, China*

Jimei Liu − *College of Materials Science & Engineering, Sichuan University, Chengdu, Sichuan 610065, China*

Bingxue Zhang − *College of Materials Science & Engineering, Sichuan University, Chengdu, Sichuan 610065, China*

Xinyu Liu − *College of Materials Science & Engineering, Sichuan University, Chengdu, Sichuan 610065, China*

Yuanjie Jiang − *College of Materials Science & Engineering, Sichuan University, Chengdu, Sichuan 610065, China*

Qinglong He − *College of Materials Science & Engineering, Sichuan University, Chengdu, Sichuan 610065, China*

Mengzhou Liao − *College of Materials Science & Engineering, Sichuan University, Chengdu, Sichuan 610065, China*; orcid.org/0000-0003-0158-0548

Yan Zhao − *College of Materials Science & Engineering, Sichuan University, Chengdu, Sichuan 610065, China*; orcid.org/0000-0002-1234-4455

https://doi.org/10.1021/acsnano.5c20704
ACS Nano 2026, 20, 14479−14487

Caofeng Pan − *Institute of Atomic Manufacturing, International Research Institute for Multidisciplinary Science, Beihang University, Beijing 100191, China*
Valeria Nicolosi − *School of Chemistry, Centre for Research on Adaptive Nanostructures and Nanodevices (CRANN) & Advanced Materials and BioEngineering Research (AMBER), Trinity College Dublin, Dublin D02W085, Ireland;* orcid.org/0000-0002-7637-4813

Complete contact information is available at: https://pubs.acs.org/10.1021/acsnano.5c20704

Notes

The authors declare no competing financial interest.

■ ACKNOWLEDGMENTS

The authors acknowledge the financial support from the National Natural Science Foundation of China (grants 00301054A1073, 22479101) and the Fundamental Research Funds for the Central Universities (grants YJ202276).

■ REFERENCES

(1) Adeyanju, I. A.; Bello, O. O.; Adegboye, M. A. Machine learning methods for sign language recognition: A critical review and analysis. *Intell. Syst. Appl.* **2021**, *12*, No. 200056.
(2) Lu, Q.; Zou, J.; Gan, Z. The Folding Hand: Anthropomorphic Robotic Hands With a Compact Reconfigurable Humanoid Palm Design. *IEEE Robot Autom. Lett.* **2025**, *10* (10), 9908−9915.
(3) Wang, M.; et al. Gesture recognition using a bioinspired learning architecture that integrates visual data with somatosensory data from stretchable sensors. *Nat. Electron.* **2020**, *3* (9), 563−570.
(4) Tashakori, A.; et al. Capturing complex hand movements and object interactions using machine learning-powered stretchable smart textile gloves. *Nat. Mach. Intell.* **2024**, *6* (1), 106−118.
(5) Kaifosh, P.; et al. A generic non-invasive neuromotor interface for human-computer interaction. *Nature* **2025**, *645* (8081), 702−711.
(6) Ali, Moin; et al. A wearable biosensing system with in-sensor adaptive machine learning for hand gesture recognition. *Nat. Electron.* **2021**, *4*, 54−63.
(7) Jiang, S.; et al. Emerging Wearable Interfaces and Algorithms for Hand Gesture Recognition: A Survey. *IEEE Rev. Bio. Eng.* **2022**, *15*, 85−102.
(8) Cheok, M. J.; Omar, Z.; Jaward, M. H. A review of hand gesture and sign language recognition techniques. *Int. J. Mach. Learn. Cyb.* **2019**, *10* (1), 131−153.
(9) Kim, K. K.; et al. A substrate-less nanomesh receptor with meta-learning for rapid hand task recognition. *Nat. Electron.* **2022**, 64−75.
(10) Yao, D.; et al. Ultrasensitive and Breathable Hydrogel Fiber-Based Strain Sensors Enabled by Customized Crack Design for Wireless Sign Language Recognition. *Adv. Funct. Mater.* **2025**, *35* (10), No. 202416482.
(11) Yang, H.; et al. A lightweight prosthetic hand with 19-DOF dexterity and human-level functions. *Nat. Commun.* **2025**, *16* (1), 955.
(12) Zhang, N.; et al. Biomimetic rigid- soft finger design for highly dexterous and adaptive robotic hands. *Sci. Adv.* **2025**, *11*, No. eadu2018.
(13) Zhang, Y.; et al. Slide ring polymer *in situ* cross-linked conductive ionogel for self-powered sensor. *Chin. Chem. Lett.* **2026**, *37* (2), No. 111676.
(14) Zhao, Z.; et al. Natural polymers-enhanced double-network hydrogel as wearable flexible sensor with high mechanical strength and strain sensitivity. *Chin. Chem. Lett.* **2023**, *34* (6), No. 107892.
(15) Wang, J.; et al. Textile-Based Strain Sensor for Human Motion Detection. *Chin. Chem. Lett.* **2020**, *3* (1), 80−100.
(16) Guo, X.; Xing, T.; Feng, J. Simultaneously Stretchable and Compressible Flexible Strain Sensors Based on Carbon Nanotube Composites for Motion Monitoring and Human−Computer Interactions. *ACS Appl. Nano Mater.* **2022**, *5* (12), 18427−18437.
(17) Bai, J.; et al. Multifunctional Flexible Sensor Based on PU-TA@MXene Janus Architecture for Selective Direction Recognition. *Adv. Mater.* **2023**, *35* (35), No. 2302847.
(18) Xie, R.; et al. Leather-Based Strain Sensor with Hierarchical Structure for Motion Monitoring. *Adv. Mater. Technol.* **2019**, *4* (10), No. 1900442.
(19) Xia, X.; et al. A conformable, durable, adhesive welded fiber mate for on-skin strain sensing. *Chem. Eng. J.* **2023**, *457*, No. 141233.
(20) Hu, B.; et al. Ultrathin crystalline silicon−based omnidirectional strain gauges for implantable/wearable characterization of soft tissue biomechanics. *Sci. Adv.* **2024**, *10* (41), No. adp8804.
(21) Lee, S.; et al. Permeable Bioelectronics toward Biointegrated Systems. *Chem. Rev.* **2024**, *124* (10), 6543−6591.
(22) Jiang, Z.; et al. A 1.3-micrometre-thick elastic conductor for seamless on-skin and implantable sensors. *Nat. Electron.* **2022**, *5*, 784−793.
(23) Shao, Y.; et al. Room-temperature high-precision printing of flexible wireless electronics based on MXene inks. *Nat. Commun.* **2022**, *13* (1), 3223.
(24) Li, D.; et al. Triphasic synthesis of MXenes with uniform and controlled halogen terminations. *Nat. Synth.* **2026**, *5*, 516.
(25) Lim, K. R. G.; et al. Fundamentals of MXene synthesis. *Nat. Synth.* **2022**, *1* (8), 601−614.
(26) Liu, Y.; et al. Ag−thiolate interactions to enable an ultrasensitive and stretchable MXene strain sensor with high temporospatial resolution. *Nat. Commun.* **2024**, *15* (1), 5354.
(27) Halim, J.; et al. X-ray photoelectron spectroscopy of select multi-layered transition metal carbides (MXenes). *Appl. Surf. Sci.* **2016**, *362*, 406−417.
(28) Sarycheva, A.; Gogotsi, Y. Raman Spectroscopy Analysis of the Structure and Surface Chemistry of $Ti_3C_2T_x$ MXene. *Chem. Mater.* **2020**, *32* (8), 3480−3488.
(29) Pu, J.; et al. Dual-Dielectric-Layer-Based Iontronic Pressure Sensor Coupling Ultrahigh Sensitivity and Wide-Range Detection for Temperature/Pressure Dual-Mode Sensing. *Adv. Mater.* **2025**, *37* (40), No. e03926.
(30) Yao, B.; et al. Stretchable Strain Sensors Based on Liquid Metal Channels with Simultaneous Significant Improvements in Linearity and Sensitivity. *Adv. Funct. Mater.* **2026**, *36*, No. 202517648.
(31) Zheng, X.; et al. A Bionic Textile Sensory System for Humanoid Robots Capable of Intelligent Texture Recognition. *Adv. Mater.* **2025**, *37* (32), No. 202417729.
(32) Zhang, C. J.; et al. Additive-free MXene inks and direct printing of micro-supercapacitors. *Nat. Commun.* **2019**, *10* (1), 1795.